Dynamical Origin of Highly Efficient Energy Dissipation in Soft Magnetic Nanoparticles for Magnetic Hyperthermia Applications

Min-Kwan Kim,[1] Jaegun Sim,[1] Jae-Hyeok Lee,[1] Miyoung Kim,[2] and Sang-Koog Kim[1],*

[1]National Creative Research Initiative Center for Spin Dynamics and Spin-Wave Devices,
Nanospinics Laboratory, Research Institute of Advanced Materials, Department of Materials Science
and Engineering, Seoul National University, Seoul 151-744, Republic of Korea
[2]Department of Materials Science and Engineering, Seoul National University,
Seoul 151-744, Republic of Korea

We explore robust magnetization-dynamic behaviors in soft magnetic nanoparticles in single-domain states and find their related high-efficiency energy-dissipation mechanism using finite-element micromagnetic simulations. We also make analytical derivations that provide deeper physical insights into the magnetization dynamics associated with Gilbert damping parameters under applications of time-varying rotating magnetic fields of different strengths and frequencies and static magnetic fields. Furthermore, we find that the mass-specific energy-dissipation rate at resonance in the steady-state regime changes remarkably with the strength of rotating fields and static fields for given damping constants. The associated magnetization dynamics are well interpreted with the help of the numerical calculation of analytically derived explicit forms. The high-efficiency energy-loss power can be obtained using soft magnetic nanoparticles in the single-domain state by tuning the frequency of rotating fields to the resonance frequency; what is more, it is controllable via the rotating and static field strengths for a given intrinsic damping constant. We provide a better and more efficient means of achieving specific loss power that can be implemented in magnetic hyperthermia applications.

I. INTRODUCTION

Magnetic nanoparticles are of increasing interest due to their unique physical properties, such as superparamagnetism [1,2], macroscopic quantum tunneling of magnetizations [3,4], the exchange-bias effect [5], and particle-size-dependent static and dynamic properties. These characteristics of magnetic nanoparticles make them very attractive for a rich variety of applications, such as high-density data storage [6,7], spintronic devices [8–10], and bioapplications including magnetic hyperthermia and magnetic-resonance-imaging contrast agents [11–14]. As an example, the magnetization dynamics of nanoparticles with vortex spin spirals exhibit unique dynamic modes such as resonant vortex-core precession motion [15] and reversals [16]. Also, soft magnetic nanoparticles in single-domain states exhibit collective Larmor precession of individual spins. In cases where the frequency of time-varying magnetic fields equals the Larmor precession frequency, individual magnetic moments efficiently absorb energies that are transferred from externally applied ac magnetic fields, after which those energies dissipate into

other forms due to their intrinsic damping of given materials. Such energy dissipations of magnetic nanoparticles are of crucial importance in low-power-consumption magnetization switching in magnetic memory devices, and also in hyperthermia bioapplications for high specific loss power (SLP) [11,12,17]. Externally applied magnetic fields in the several-hundred-kilohertz range can be absorbed by magnetic nanoparticles and then dissipated via Brownian rotation of the nanoparticles and/or Néel relaxation [1] of the magnetizations inside them [18,19]. It has been reported that the SLP for the aforementioned mechanisms ranges between 0.5 and 2 kW/g. Contrastingly, Larmor precession motions of individual spins in magnetic particles excited by relatively high-frequency (several-hundred-megahertz) ac magnetic fields can give rise to high-efficiency energy dissipation into a different form of energy (e.g., heat). Thus, their mechanism-related SLP would be higher than those of other mechanisms.

In this work, we explore robust nonlinear magnetization dynamics and the associated high-efficiency energy-dissipation effect in soft magnetic nanospheres in single-domain states, as excited by oscillating magnetic fields of different frequencies and amplitudes under given static magnetic fields. We conduct micromagnetic simulations to explore the magnetization

*To whom all correspondence should be addressed.
sangkoog@snu.ac.kr

dynamics of soft magnetic particles and additional analytical derivations of the energy-dissipation rate for the steady-state regime by varying the frequency and strength of rotating magnetic fields for different Gilbert damping constants and static magnetic field strengths. All of the simulation results and analytical calculations agree well quantitatively. The dynamic origin of such a high-efficiency energy-dissipation mechanism is completely different from those of the typical ones used in bioapplications. We expect that this efficient, very high energy-dissipation rate will prove implementable in magnetic hyperthermia applications.

The paper is organized as follows. In Sec. II, we describe our modeling and relevant micromagnetic simulations. The dynamic characteristic motions of magnetizations and magnetic torque terms numerically calculated from the micromagnetic simulation data for nonresonant and resonant cases are described in Sec. III, as are the corresponding analytical calculations in Sec. IV. The energy-dissipation rate of single-domain nanospheres obtained from the micromagnetic simulations is given in Sec. V, and the analytical derivations are provided in Sec. VI. The maximum value of the resonant energy-dissipation rate also is calculated and compared to those obtained from other models in terms of typical SLP in the field of magnetic hyperthermia applications. We summarize our findings in Sec. VII.

II. MICROMAGNETIC SIMULATIONS

In this paper, we conduct finite-element micromagnetic simulations of soft magnetic permalloy (Py, $Ni_{80}Fe_{20}$) nanospheres in single-domain states, the diameters of which are set to $2R = 10$, 20, and 30 nm. To numerically solve dynamic motions of magnetizations ($\mathbf{M}$, a vector quantity), we use the FEMME code (version 5.0.9) [20] that utilizes the Landau-Lifshitz-Gilbert (LLG) equation

$$\frac{d\mathbf{M}}{dt} = -\gamma[\mathbf{M} \times \mathbf{H}_{\text{eff}}] + \frac{\alpha}{M_s}\left[\mathbf{M} \times \frac{d\mathbf{M}}{dt}\right], \quad (1)$$

where $\mathbf{H}_{\text{eff}}$ is the effective field, M_s is the saturation magnetization value, α is the dimensionless Gilbert damping constant, and γ is the gyromagnetic ratio. The effective field consists of the exchange, the magnetostatic, the magnetocrystaline anisotropy, and Zeeman fields. The magnetic parameters corresponding to the Py material are as follows: saturation magnetization $M_s = 860$ emu/cm^3, exchange stiffness $A = 1.3 \times 10^{-6}$ erg/cm, gyromagnetic ratio $\gamma = 2\pi \times 2.8$ rad MHz/Oe, and zero magnetocrystalline anisotropy. To avoid errors inherent to representation of a spherical geometry with a set of polyhedron cells, we discretize the surfaces of the nanospheres into triangles of roughly equal area using hierachical triangular mesh [21], and the inner volume into tetrahedron elements (mesh size ≤ 3 nm) [see Fig. 1(a)].

(a)

$2R$ (nm)
= 10, 20, and 30

(b)
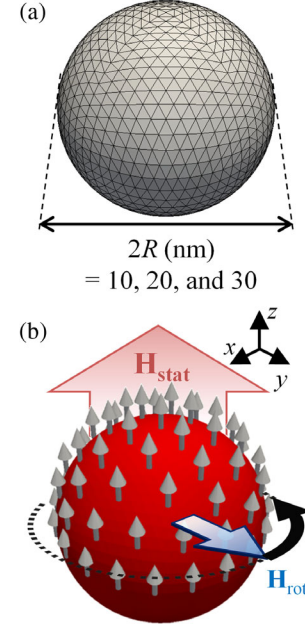
FIG. 1. (a) Finite-element sphere model of diameter $2R = 10$–30 nm. (b) Single-domain sphere model of diameter $2R = 20$ nm under a circular-rotating field and a static field.

Through relaxation from initially saturated magnetizations oriented in the $+z$ direction for the Py nanospheres, we obtain uniformly magnetized single-domain ground states for each diameter: $2R = 10$, 20 [Fig. 1(b)], and 30 nm. For the Py spheres, the single-domain states are maintained up to $2R = 35$ nm as a result of competition between strong exchange (short-range) and weak dipole-dipole (long-range) interactions in such nanoscale geometrical confinements. Because the spheres are magnetically isotropic insofar as there are no other sources of anisotropy [22], uniform magnetizations can reorient to the direction of applied static magnetic fields. It is well known that such single-domain magnetic particles exhibit collective Larmor precession motions of individual spins around the axis of a static magnetic field with characteristic frequency [15]. Ferromagnetic resonance [22,23] occurs in such a single-domain magnetic particle as a collective precession motion of individual spins around the static magnetic-field axis. In a given isotropic system, the resonance frequency is given as

$$f_L = (\gamma/2\pi)H_{\text{dc}}, \quad (2)$$

where H_{dc} is the static field strength [15,23]. Note that the resonance frequency of the magnetic thin film changes with the axis about which the magnetizations precess, but the resonance frequency of sphere model $f_L = (\gamma/2\pi)H_{\text{dc}}$ does not change with the magnetization orientation because the demagnetization field in the sphere model is the same

for all field directions and for the precession of the uniform magnetizations [22].

III. CHARACTERISTIC DYNAMIC MOTIONS

To investigate the Py nanospheres' characteristic modes of coherent magnetization dynamics, we apply a static field $\mathbf{H}_{\text{stat}} = H_{\text{dc}}\hat{\mathbf{z}}$ in the $+z$ direction, which allows for the reorientation of the magnetizations in the $+z$ direction. Since the Larmor precession motion of magnetizations is counterclockwise (CCW) in its rotation sense, we choose the CCW basis of circular-rotating magnetic fields on the x-y plane, as described by $\mathbf{H}_{\text{rot}} = H_{\text{ac}} \cos(2\pi f_{\text{CCW}}t)\hat{\mathbf{x}} + H_{\text{ac}} \sin(2\pi f_{\text{CCW}}t)\hat{\mathbf{y}}$, with the field strength H_{ac} and the field frequency f_{CCW} [see Fig. 1(b)]. For $2R = 20$ nm under $H_{\text{dc}} = 100$ Oe, Fig. 2 shows the characteristic precession motions' unit vector $\mathbf{m} = \mathbf{M}/M_s$ of the uniform magnetizations excited by three different frequencies, $f_{\text{CCW}} = 200$, 280, and 360 MHz, where $H_{\text{ac}} = 4$, 5, and 6 Oe, respectively. Since the Larmor frequency for the Py sphere of

FIG. 2. Temporal evolution of x, y, and z components of $\mathbf{m}$ for different strengths of circular-rotating fields $H_{\text{ac}} = 4$, 5, and 6 Oe for (a) a nonresonant case ($f_{\text{CCW}} = 200$ MHz), (b) a resonant case ($f_{\text{CCW}} = 280$ MHz), and (c) a nonresonant case ($f_{\text{CCW}} = 360$ MHz). (d) f_{rev} obtained by a FFT of the simulation results of m_z as a function of H_{ac}. The symbols with the black solid line denote the micromagnetic simulation results, while the red solid lines correspond to $f_{\text{rev}} = (\gamma/2\pi)H_{\text{ac}}$. The static field strength $H_{\text{dc}} = 100$ Oe and damping constant $\alpha = 0.05$ are used for all of the simulations shown in this figure.

$2R = 20$ nm under a given field strength of $H_{\text{dc}} = +100$ Oe is equal to $f_L = 280$ MHz, in accordance with Eq. (2), the application of $f_{\text{CCW}} = 200$ and 360 MHz would lead to nonresonant excitations, whereas the application of $f_{\text{CCW}} = 280$ MHz leads to resonant excitations. At non-resonance excitations [see Figs. 2(a) and 2(c)], the in-plane m_x and m_y components are small, while m_z is almost close to unity, indicating that the precession motions of the magnetizations occur while keeping $\mathbf{m}$ in the $+z$ direction. On the other hand, at resonance excitations [see Fig. 2(b)], the precession motions occur with relatively large in-plane $\mathbf{m}$ components, even for the very small field strengths of $H_{\text{ac}} = 4$, 5, and 6 Oe. All of the dynamic motions for the individual cases finally reach their corresponding steady states with specific m_z values according to the given H_{ac} value. All of the m_z values in the steady states also decrease with increasing H_{ac} values until $H_{\text{ac}} = 5$ Oe. Beyond the field magnitude $H_{\text{ac}} = 5$ Oe, the m_z value becomes zero, indicating that all of the final steady states are in the precession motion of $\mathbf{m}$ on the x-y plane, i.e., the equator of the sphere. On the other hand, at $H_{\text{ac}} = 6$ Oe, for example, the $\mathbf{m}$ periodically oscillates (switches) between the $+z$ and $-z$ directions before converging to the precession motion exactly on the equator, i.e., keeping $m_z = 0$. It is interesting to further examine the frequency of the $\mathbf{m}$ switching with varying H_{ac} values, as shown in Fig. 2(d). As evident from the simulation results (the symbols), the periodic switching of $\mathbf{m}$ starts when H_{ac} reaches αH_{dc} for given values of H_{dc} and α. The existence of a threshold field strength $H_{\text{ac}}^{\text{th}} = \alpha H_{\text{dc}}$ is explained below according to the steady-state torque balance. For the cases where $H_{\text{ac}} \gg \alpha H_{\text{dc}}$, the dynamics are characterized by the fact that the reversal frequency f_{rev} is proportional to H_{ac}, as expressed by $f_{\text{rev}} = (\gamma/2\pi)H_{\text{ac}}$ (indicated by the red solid line).

A. Torque balance interpretation

In order to understand the distinct dynamic motions occurring for different H_{ac} values, we take into account the magnetic torque balance. As shown in Fig. 3(a), the static field $\mathbf{H}_{\text{stat}}$ acting on $\mathbf{m}$ leads to the static field torque $\boldsymbol{\tau}_{\text{stat}}$ that allows for the precession of magnetizations around the static field. The rotating field $\mathbf{H}_{\text{rot}}$ results in the torque $\boldsymbol{\tau}_{\text{rot}}$ that determines the direction of $\mathbf{m}$ with respect to the static field direction in balance with the intrinsic damping torque $\boldsymbol{\tau}_{\text{damp}}$ [see Fig. 3(a)]. The torque balance equation can be derived from the LLG equation as

$$\boldsymbol{\tau}_{\text{stat}} = -\mathbf{m} \times \mathbf{H}_{\text{stat}},$$

$$\boldsymbol{\tau}_{\text{rot}} = -\mathbf{m} \times \mathbf{H}_{\text{rot}},$$

$$\boldsymbol{\tau}_{\text{damp}} = \frac{\alpha}{\gamma}\mathbf{m} \times \frac{d\mathbf{m}}{dt}. \qquad (3)$$

Here, we consider only the external magnetic fields for $\mathbf{H}_{\text{eff}}$ because, for a single-domain spherical nanoparticle,
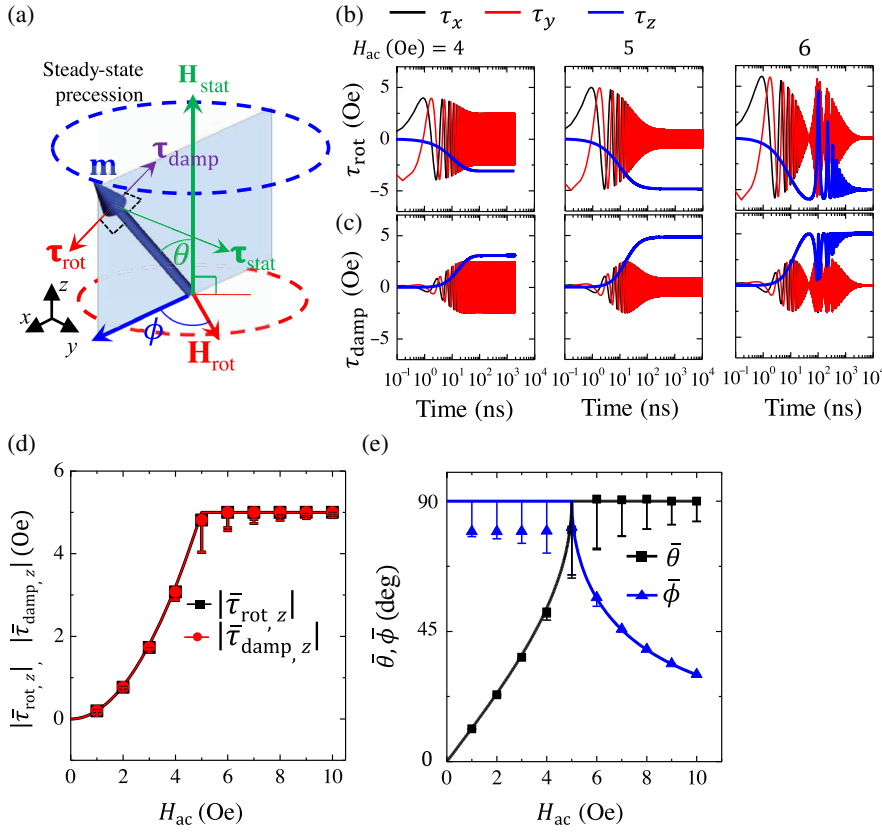
FIG. 3. (a) Schematic illustration of dynamic relationship between the macrospin (uniform magnetization) and the external static field and time-varying circular-rotating field. $\mathbf{H}_{rot}$ is always on the plane perpendicular to the static field direction. The spherical angles for magnetization vector $\mathbf{m}$ are defined in the figure; θ is measured in respect to $\mathbf{H}_{stat}$ and ϕ in respect to $\mathbf{H}_{rot}$. The directions of the principal torque vectors $\boldsymbol{\tau}_{stat}, \boldsymbol{\tau}_{rot}$, and $\boldsymbol{\tau}_{damp}$ are also shown. Temporal evolution of the x (black), y (red), and z (blue) components of (b) $\boldsymbol{\tau}_{rot}$ and (c) $\boldsymbol{\tau}_{damp}$ for different strengths of circular-rotating fields $H_{ac} = 4$, 5, and 6 Oe in a resonant case ($f_{CCW} = 280$ MHz). (d) Steady-state values of z components of $|\boldsymbol{\tau}_{rot}|$ and $|\boldsymbol{\tau}_{damp}|$ as a function of H_{ac}. (e) Steady-state values of θ and ϕ as functions of H_{ac}. The symbols denote the micromagnetic simulation results, while the solid lines correspond to the analytical calculation data. The static field strength $H_{dc} = 100$ Oe and damping constant $\alpha = 0.05$ are used for all of the simulations shown in this figure. The error bars of the simulation values of the torques and angles are plotted for possible $\pm 1\%$ errors that could occur in the micromagnetic simulation.

neither the exchange field nor the demagnetization field varies with the orientation of $\mathbf{m}$. The torque term $\boldsymbol{\tau}_{stat}$ has no effect in determining the z component torque balance because it is always on the x-y plane; consequently, its z component is absent. Therefore, the z-component torque balance in the steady state always holds for the condition $\bar{\boldsymbol{\tau}}_{rot,z} + \bar{\boldsymbol{\tau}}_{damp,z} = 0$. Hereafter, the bar over the symbols indicates the value corresponding to the steady state of the system. According to Eq. (3) and the temporal magnetization variation obtained in the simulations, we calculate [see Fig. 3(b)] the x, y, and z components of $\boldsymbol{\tau}_{rot}$ and $\boldsymbol{\tau}_{damp}$ as a function of time for different values of $H_{ac} = 4$, 5, and 6 Oe for the given values of $2R = 20$ nm, $H_{dc} = 100$ Oe, and $\alpha = 0.05$, and the resonance excitation $f_{CCW} = f_L = 280$ MHz, under the same conditions as are shown in Fig. 2(b). Hereafter, we focus on only the z-component torques because they determine the m_z values in the steady states during their precession motions. The $|\boldsymbol{\tau}_{rot,z}|$ value for $H_{ac} = 4$ and 5 Oe continuously increases with time and then reaches its steady-state value, $|\bar{\boldsymbol{\tau}}_{rot,z}|$. However, as for $H_{ac} = 6$, $|\boldsymbol{\tau}_{rot,z}|$ gradually increases and reaches its maximum value, then starts to oscillate with its large amplitude. This large oscillation of $\boldsymbol{\tau}_{rot,z}$ finally converges to its steady-state value, $\bar{\boldsymbol{\tau}}_{rot,z}$. Also, $\boldsymbol{\tau}_{damp,z}$ shows similar behaviors as $\boldsymbol{\tau}_{rot,z}$ does, but the signs are opposites. In the case of steady-state magnetization dynamics, $\bar{\boldsymbol{\tau}}_{rot,z}$ and $-\bar{\boldsymbol{\tau}}_{damp,z}$ balance each other. Since $|\boldsymbol{\tau}_{rot,z}|$ and $|\bar{\boldsymbol{\tau}}_{damp,z}|$ vary with H_{ac}, it is

worthwhile to plot their relation as in Fig. 3(d). $|\bar{\boldsymbol{\tau}}_{rot,z}|$ increases with H_{ac} until H_{ac} approaches the value of αH_{dc}, then reaches its saturation value even with a further increase above the specific field strength $H_{ac}^{th} = \alpha H_{dc}$. This threshold field strength is already shown in the relation of f_{rev} versus H_{ac} [see Fig. 2(c)]. On the basis of the steady-state torque balance, we obtain the angles $\bar{\theta}$ and $\bar{\phi}$ defined in Fig. 3(e) as a function of H_{ac}. In the cases where $H_{ac} \geq \alpha H_{dc}$, $\bar{\theta}$ always is maintained at 90°, indicating the processional motion of $\mathbf{m}$ on the x-y plane (the equator). For $H_{ac} < \alpha H_{dc}$, $\mathbf{m}$ and the rotating field vector are not coplanar with respect to the plane of $\mathbf{m}$ and the static field, as shown in Fig. 3(a). However, as H_{ac} is much larger than the threshold field strength $H_{ac}^{th} = \alpha H_{dc}$, $\mathbf{m}$ rotates coherently with $\mathbf{H}_{rot}$ on the x-y plane.

IV. ANALYTICAL DERIVATION OF MAGNETIZATION DYNAMICS

To understand the underlying physics of the magnetization dynamics and associated torque behaviors obtained from the micromagnetic simulations, we additionally derive analytical forms from the LLG equation. By multiplying $\mathbf{m}$ on both sides of Eq. (1), we obtain

$$\frac{d\mathbf{m}}{dt} = -\gamma'[\mathbf{m} \times \mathbf{H}_{ext}] + \gamma'\alpha[[\mathbf{m} \times \mathbf{H}_{ext}] \times \mathbf{m}], \quad (4)$$

with $\gamma' = \gamma/(1 + \alpha^2)$, where $\mathbf{H}_{\mathrm{ext}}$ is composed of the rotating field on the x-y plane and the static field applied in the $+z$ direction. Since the $\mathbf{m}$ vector precesses about the z axis, it is convenient to transform the time-varying $\mathbf{m}$ vector into its time-independent counterpart $\mathbf{u}$ vector on the same rotating frame on the x-y plane, as $\mathbf{u} = \mathbb{N}\mathbf{m}$, with the following transformation matrix [24–27]:

$$\mathbb{N} = \begin{pmatrix} \cos(\omega_{\mathrm{CCW}}t) & \sin(\omega_{\mathrm{CCW}}t) & 0 \\ -\sin(\omega_{\mathrm{CCW}}t) & \cos(\omega_{\mathrm{CCW}}t) & 0 \\ 0 & 0 & 1 \end{pmatrix}. \quad (5)$$

By inserting the relation of $\mathbf{u} = \mathbb{N}\mathbf{m}$ into Eq. (4), the x, y, and z components of the $\mathbf{u}$ vector are solved as

$$u_x = \frac{1 - u_z^2}{\gamma H_{\mathrm{ac}} u_z}(\omega_L - \omega_{\mathrm{CCW}}),$$
$$u_y = -\frac{\alpha\omega_{\mathrm{CCW}}}{\gamma H_{\mathrm{ac}}}(1 - u_z^2), \quad (6)$$

with $\omega_{\mathrm{CCW}} = 2\pi f_{\mathrm{CCW}}$ and $\omega_L = 2\pi f_L = \gamma H_{\mathrm{dc}}$. With $u_x^2 + u_y^2 + u_x^2 = 1$, we get the relation

$$(\gamma H_{\mathrm{ac}})^2 = \frac{(1 - u_z^2)}{u_z^2}[(\omega_L - \omega_{\mathrm{CCW}})^2 + (\alpha\omega_{\mathrm{CCW}}u_z)^2]. \quad (7)$$

Then, finally, it becomes

$$u_z^2 = \frac{-[\gamma^2 H_{\mathrm{ac}}^2 - \alpha^2\omega_{\mathrm{CCW}}^2 + (\omega_L - \omega_{\mathrm{CCW}})^2] + \sqrt{[\gamma^2 H_{\mathrm{ac}}^2 - \alpha^2\omega_{\mathrm{CCW}}^2 + (\omega_L - \omega_{\mathrm{CCW}})^2]^2 + [2\alpha\omega_{\mathrm{CCW}}(\omega_L - \omega_{\mathrm{CCW}})]^2}}{2\alpha^2\omega_{\mathrm{CCW}}^2}.$$

$$(8)$$

Under the resonance condition of $f_{\mathrm{CCW}} = f_L$, the u_z simply is given as the two different ranges of H_{ac}:

$$u_z^2 = 1 - \left(\frac{H_{\mathrm{ac}}}{\alpha H_{\mathrm{dc}}}\right)^2, \qquad H_{\mathrm{ac}} < \alpha H_{\mathrm{dc}}, \quad (9a)$$

$$u_z^2 = 0, \qquad H_{\mathrm{ac}} \geq \alpha H_{\mathrm{dc}}. \quad (9b)$$

Through the relation $\mathbf{u} = \mathbb{N}\mathbf{m}$, we obtain $\bar{m}_x$, $\bar{m}_y$, and $\bar{m}_z$ again as

$$\bar{m}_x = u_x \cos(\omega_{\mathrm{CCW}}t) - u_y \sin(\omega_{\mathrm{CCW}}t),$$
$$\bar{m}_y = u_x \sin(\omega_{\mathrm{CCW}}t) + u_y \cos(\omega_{\mathrm{CCW}}t),$$
$$\bar{m}_z = u_z. \quad (10)$$

Accordingly, the z components of the toque terms in the steady state at resonance are represented by $\bar{\tau}_{\mathrm{rot},z} = -H_{\mathrm{ac}}\sin(\bar{\theta})\sin(\bar{\phi})$ and $\bar{\tau}_{\mathrm{damp},z} = \alpha H_{\mathrm{dc}}\sin^2(\bar{\theta})$, with $\bar{\theta} = \arccos(u_z)$ and $\bar{\phi} = \arccos[u_x/\sin(\bar{\theta})]$. The analytical calculations of the torques are in excellent agreement with the micromagnetic simulation results (the symbols), as shown in Fig. 3(e). We also plot the steady-state angles of $\bar{\theta}$ and $\bar{\phi}$ as a function of H_{ac}, as shown in Fig. 3(e). In the range of $H_{\mathrm{ac}} < \alpha H_{\mathrm{dc}}$, $\bar{\theta}$ increases with H_{ac} up to 90°. We note that $\bar{\theta} = 90°$ corresponds to the precession of uniform magnetizations on the x-y plane (the equator) with $m_z = 0$. The above analytical forms (the solid lines) inform us how the steady-state torques change with H_{ac} and why the torque has its maximum value of αH_{dc}, which is independent of H_{ac} above the threshold field strength $H_{\mathrm{ac}} = \alpha H_{\mathrm{dc}}$. In the case where $H_{\mathrm{ac}} < H_{\mathrm{ac}}^{\mathrm{th}} = \alpha H_{\mathrm{dc}}$, $\bar{\phi}$ is almost 90°, and thus $\bar{\theta}$ is given by $\bar{\theta} = \arcsin(H_{\mathrm{ac}}/\alpha H_{\mathrm{dc}})$, as indicated by the black solid line in Fig. 3(e). For the cases where $H_{\mathrm{ac}} \geq \alpha H_{\mathrm{dc}}$, the torque balance leads to $\bar{\theta} = 90°$ and, consequently, to $\bar{\phi} = \arcsin(\alpha H_{\mathrm{dc}}/H_{\mathrm{ac}})$. This means that, for the cases where $H_{\mathrm{ac}}/H_{\mathrm{ac}}^{\mathrm{th}} \gg 1$, $\mathbf{m}$ rotates coherently with the rotating field on the x-y plane. The torque balance equations well explain the steady-state dynamics observed in this paper. In Fig. 3(e), the micromagnetic simulation results of $\bar{\phi}$ and the corresponding analytical calculation values show a large discrepancy because $\bar{\phi}$ is very sensitive to small errors in other parameters obtained from the simulation. Here, we note that the analytical calculation of $\bar{\phi}$ coincides with the corresponding simulation results within the error bars. The error bars indicated in Fig. 3(e) are calculated assuming a $\pm 1\%$ error in the choice of resonant frequency f_{CCW} because a $\pm 1\%$ error of f_{CCW} can lead to a major error in the numerical calculation of $\bar{\phi}$.

V. ENERGY DISSIPATION

Above, we explore both the nonresonant and resonant dynamic motions of the magnetizations of Py nanospheres in single-domain states. The robust dynamics of soft magnetic nanoparticles in nonlinear dynamic regimes can be implemented in magnetic hyperthermia applications. In the research field of magnetic hyperthermia, SLP in the form of watts per gram (W/g) is widely used to represent heat (or temperature increase) from magnetic particles. On the basis of energy conservation and fundamental Maxwell equations, the power loss can be represented by the magnetic energy-dissipation rate, and it can be expressed as [28]

$$Q = -\frac{1}{\rho V} \int_V [d\varepsilon_G/dt + \mathbf{M}(t) \cdot d\mathbf{H}_{\mathrm{ext}}(t)/dt] dV, \quad (11)$$

where ε_G is the Gibbs energy density with the volume of nanosphere V and the density of permalloy $\rho = 8.72 \, \mathrm{g/cm^3}$. The first and second terms on the right side are the time derivative of magnetic energy and the dual power of external force, respectively (for further details, see Ref. [28]). In the current research on magnetic hyperthermia, oscillating magnetic fields of a few hundred kilohertz are typically applied; therefore, the SLP, as a measurable quantity, is redefined to Q averaged over a time period T_0,

$$\langle Q \rangle = -\frac{1}{\rho V T_0} \int_0^{T_0} \int_V [d\varepsilon_G/dt + \mathbf{M}(t) \cdot d\mathbf{H}_{\mathrm{ext}}(t)/dt] dV dt$$

$$(12)$$

Accordingly, from our micromagnetic simulation data, we can directly obtain the quantities of Q and $\langle Q \rangle$ versus a given time for the nonlinear dynamic motions of a single-domain nanosphere of $2R = 20$ nm for the specific cases of $H_{\mathrm{dc}} = 100$ Oe and $\alpha = 0.05$, as excited by three different frequencies, $f_{\mathrm{CCW}} = 200$ and 360 MHz (off resonance) and 280 MHz (resonance), for the values $H_{\mathrm{ac}} = 4$, 5, and 6 Oe, respectively. Whether at resonance or off resonance, the two different quantities of Q and $\langle Q \rangle$ display somewhat distinct behaviors for most of the time, except for their steady states, as shown in Fig. 4. For example, in the case of off resonance, there are large differences between Q and $\langle Q \rangle$, whereas those values became almost equal above $t = 100$ ns. In the case of resonance, the steady state wherein both values become equal is achieved after a rather long time, above 1500 ns. The reason for the equal values of Q and $\langle Q \rangle$ in the steady states is the fact that the $\partial \varepsilon_G / \partial t$ term in both Q and $\langle Q \rangle$ becomes zero, so that Q and $\langle Q \rangle$ are the same. Although the $\langle Q \rangle$ quantity typically represents the measurable SLP, in this paper, we use the quantity of Q because it can be calculated analytically for a comparison with the corresponding simulation.

Related to the above issue regarding SLP, from now on, we focus only on Q values that (1) can be numerically calculated from the micromagnetic simulation data shown in Fig. 4 using Eq. (11), and (2) can be analytically derived, as we show later. Figure 5 compares the individual Q values, as well as the negative derivative of energy density $-[1/(\rho V)]\int_V (d\varepsilon_G/dt) dV$ and the negative dual power density $-[1/(\rho V)]\int_V (d\mathbf{H}_{\mathrm{ext}}/dt \cdot \mathbf{M}) dV$ calculated from the simulation results for the nonresonant ($f_{\mathrm{CCW}} = 200$ and 360 MHz) and resonant ($f_{\mathrm{CCW}} = f_L = 280$ MHz) conditions.

At nonresonance, those values largely fluctuate up to 10 ns, after which they reach their steady-state regime. These large oscillations are associated with the initial large perturbations of magnetizations, as shown in Figs. 2(a)
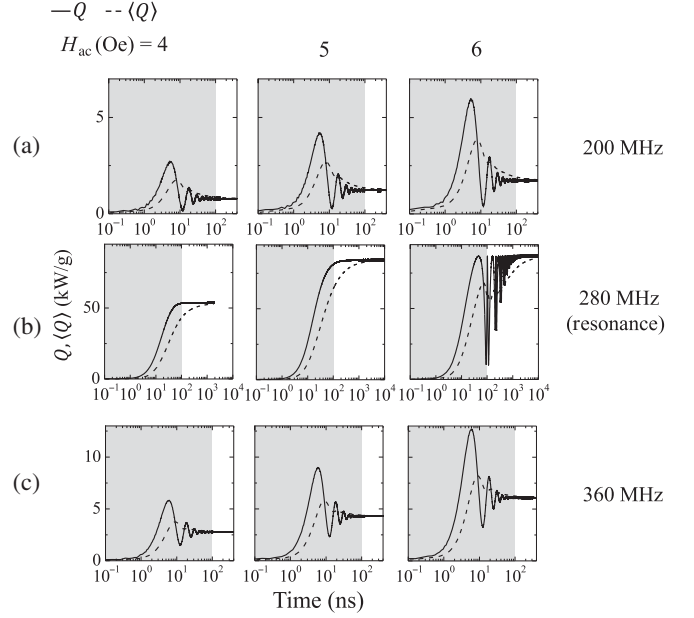
FIG. 4. Temporal evolution of energy-dissipation rate, Q (the solid line), and its time average $\langle Q \rangle$ (the dashed line) for excitation of Py nanosphere of diameter $2R = 20$ nm by $H_{\mathrm{ac}} = 4$, 5, and 6 Oe, $H_{\mathrm{dc}} = 100$ Oe, and $\alpha = 0.05$, for (a) a nonresonant case ($f_{\mathrm{CCW}} = 200$ MHz), (b) a resonant case ($f_{\mathrm{CCW}} = 280$ MHz), and (c) a nonresonant case ($f_{\mathrm{CCW}} = 360$ MHz). The intervals between 0.1 and 100 ns are distinguished by the gray shading.

and 2(c). On the contrary, at resonance, the values of Q and $-[1/(\rho V)]\int_V (d\mathbf{H}_{\mathrm{ext}}/dt \cdot \mathbf{M}) dV$ slowly increase and then converge to certain corresponding values due to the fact that their dynamic motions reach their corresponding steady states. For all of the cases, the $-[1/(\rho V)] \times \int_V (d\varepsilon_G/dt) dV$ (the black line) converges to zero in the steady states, but $-[1/(\rho V)]\int_V (d\mathbf{H}_{\mathrm{ext}}/dt \cdot \mathbf{M}) dV$ (in red) becomes equal to Q; hereafter, the Q quantity in the steady state is noted as $\bar{Q}$. Therefore, $\bar{Q}$ is determined only by the dual power density. $\bar{Q}$ values for the nonresonant and resonant cases contrast starkly. For the nonresonant condition, those energy powers relatively quickly converge to zero or low values after large initial fluctuations. As H_{ac} increases, the initial oscillations and steady-state values increase. By contrast, at resonance, the initial oscillations disappear, but the time derivatives of energy density and dual power density converge to certain values after a longer time (as late as 1000 ns). Also, using an H_{ac} value larger than 5 Oe—for example, 6 Oe—those energy powers oscillate with large fluctuations before reaching the steady state, whose oscillations are related to magnetization switching between the $+z$ and $-z$ directions, as shown in Fig. 2.

The quantities of $\bar{Q}$ at resonance are much higher than those at nonresonance. In order to compare $\bar{Q}$ as a function of f_{CCW}, we conduct micromagnetic simulations
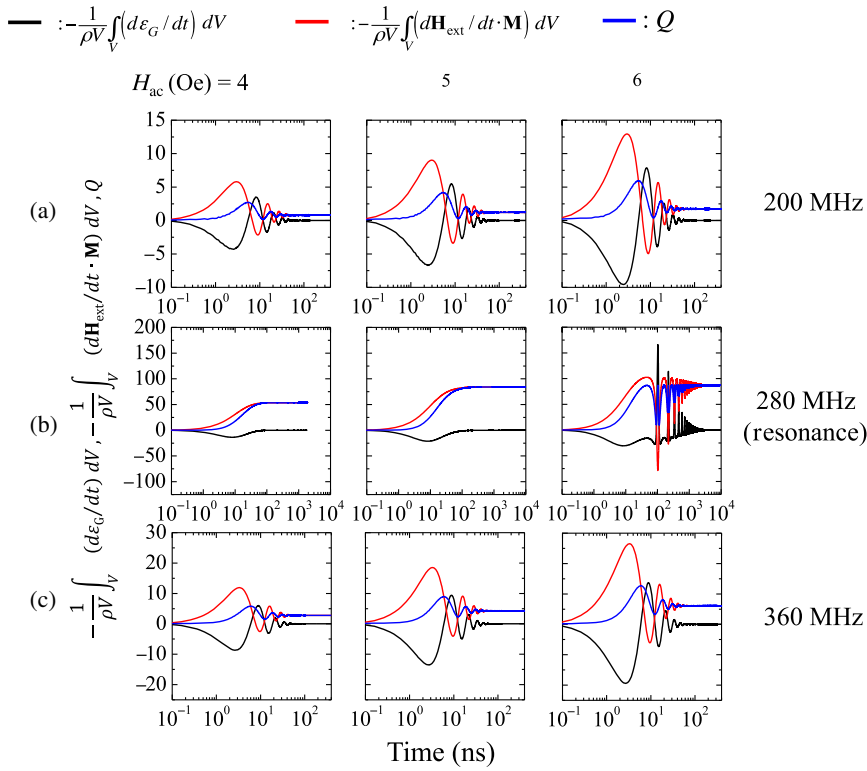
FIG. 5. Temporal evolution of the energy-dissipation rate (the blue lines), the negative dual power density (the red lines), and the negative time derivative of total energy density (the black lines) for excitation of a Py nanosphere of diameter $2R = 20$ nm by $H_{ac} = 4$, 5, and 6 Oe, $H_{dc} = 100$ Oe, and $\alpha = 0.05$, for (a) a nonresonant case ($f_{CCW} = 200$ MHz), (b) a resonant case ($f_{CCW} = 280$ MHz), and (c) a nonresonant case ($f_{CCW} = 360$ MHz).

by varying f_{CCW} in the (20–540)-MHz range; then, from the simulation results, we numerically calculate $\bar{Q}$ versus f_{CCW}. As shown in Fig. 6, under the application of $H_{dc} = 100$ Oe and $H_{ac} = 5$ Oe, we plot $\bar{Q}$ values versus f_{CCW} for

the values of $\alpha = 0.01$, 0.03, 0.05, and 0.07, and for Py nanospheres of $2R = 10$, 20, and 30 nm in single-domain states. As is apparent, there are clear peaks when f_{CCW} reaches f_L (=280 MHz), independent of α. These results
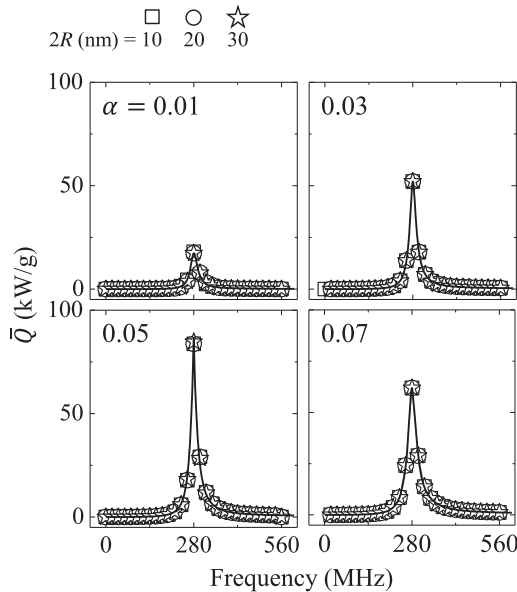
FIG. 6. Energy-dissipation rate in the steady-state regime as a function of frequency of circular-rotating fields for excitation of Py nanospheres of diameter $2R = 10$, 20, and 30 nm with $H_{ac} = 5$ Oe, $H_{dc} = 100$ Oe, and $\alpha = 0.01$, 0.03, 0.05, and, 0.07. The symbols and lines represent the micromagnetic simulation and analytical calculation results, respectively.
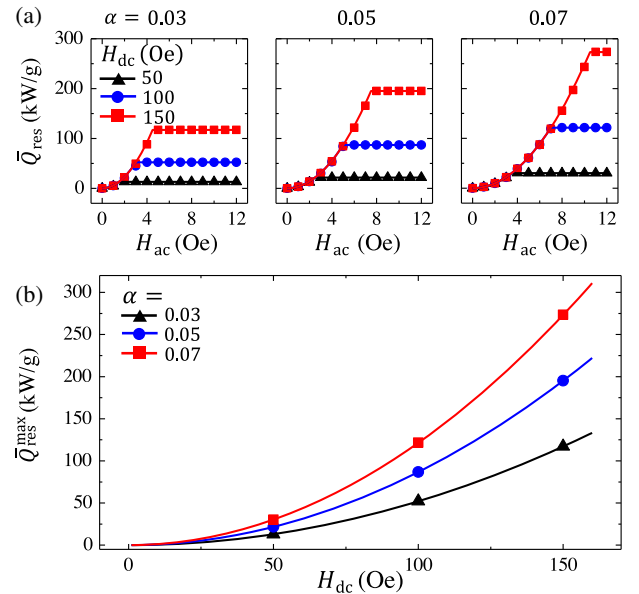
FIG. 7. (a) Steady-state energy-dissipation rate at corresponding resonance frequencies as a function of H_{ac} for $2R = 20$ nm with different static field strengths ($H_{dc} = 50$, 100, 150 Oe) for given damping constants ($\alpha = 0.03$, 0.05, and 0.07). (b) Maximum energy-dissipation rate versus H_{dc} for given damping constants. The symbols and lines indicate the micromagnetic simulation and analytical calculation results, respectively.

indicate that the energy forms of the applied magnetic fields are transferred highly efficiently to nanoparticles and then subsequently dissipate via nonlinear magnetization dynamics due to intrinsic damping.

Such a high quantity of $\bar{Q}$ at resonance is important in terms of the efficient energy transfer of external magnetic-field energy to a magnetic sphere and the subsequent release into other energy forms such as heat via dynamic magnetization dissipation. Also, since magnetic particles can be applicable to hyperthermia bioapplications, it is worth examining, for resonance cases, $\bar{Q}$ versus H_{ac} for different H_{dc} fields and values of α. From further micromagnetic simulations, we obtain $\bar{Q}$ at resonance (hereafter noted as $\bar{Q}_{res}$) versus H_{ac} for the three virtual cases of $\alpha = 0.03$, 0.05, and 0.07, and for the values of $H_{dc} = 50$,

100, and 150 Oe. For the given values of α, $\bar{Q}_{res}$ increases with H_{ac} up to a certain value of H_{ac} (noted as H_{ac}^{th}), thereafter becoming saturated even with a further increase of H_{ac} beyond H_{ac}^{th} [Fig. 7(a)]. Quite interestingly, H_{ac}^{th} varies with H_{dc} and α. Also, the saturated quantity of $\bar{Q}_{res}$, $\bar{Q}_{res}^{max}$ increases with H_{dc} as well as α, as shown in Fig. 7(b). The underlying physics of these micromagnetic simulation results (the symbols) are now explained with the help of an analytical derivation.

VI. ANALYTICAL DERIVATION OF $\bar{Q}$

As shown by the simulation results (see Fig. 6), $\bar{Q}$ can be simply determined from the dual power in the steady state, assuming $d\varepsilon_G/dt = 0$:

$$\bar{Q} = \frac{M_s H_{ac} \omega_{CCW}}{\rho}(-u_y)$$
$$= \frac{M_s}{2\rho\gamma\alpha}\left[(\gamma H_{ac})^2 + (\alpha\omega_{CCW})^2 + (\omega_L - \omega_{CCW})^2 - \sqrt{[(\gamma H_{ac})^2 - (\alpha\omega_{CCW})^2 + (\omega_L - \omega_{CCW})^2]^2 + [2\alpha\omega_{CCW}(\omega_L - \omega_{CCW})]^2}\right].$$

$$(13)$$

From the analytical form of $\bar{Q}$, it is clear that $\bar{Q}$ is a function of $\omega_{CCW} = 2\pi f_{CCW}$, H_{ac}, H_{dc}, and α because of $\omega_L = \gamma H_{dc}$. Thus, for a given material, the external field parameters of H_{dc} and H_{ac}, as well as f_{CCW}, determine the value of $\bar{Q}$. Using Eq. (13), we numerically calculate the $\bar{Q}$ versus f_{CCW} behaviors (the solid lines) for single-domain-state Py nanospheres of $2R = 10$, 20, and 30 nm in the following cases: $H_{dc} = 100$ Oe, $H_{ac} = 5$ Oe, and $\alpha = 0.01$, 0.03, 0.05, and 0.07. As shown in Fig. 6, the analytical derivations are in excellent agreement with the micromagnetic simulation results (the symbols). Moreover, the maximum values of $\bar{Q}$ are found at $f_{CCW} = 280$ MHz, which corresponds to the Py nanospheres' Larmor frequency expressed as $f_L = (\gamma/2\pi)H_{dc}$. The Larmor frequency in the case of single-domain-state nanoparticles does not change with $2R$, as reported in Ref. [15]. Note that the largest quantity of $\bar{Q}$ is obtained at resonance by tuning f_{CCW} to f_L.

To gain deeper physical insight into the relations of $\bar{Q}_{res}$ with H_{ac}, H_{dc}, and α, as observed from the micromagnetic simulations shown in Fig. 7, we obtain the analytical forms of $\bar{Q}_{res}$ by inserting $f_{CCW} = f_L$ into Eq. (13):

$$\bar{Q}_{res} = \frac{1}{\alpha}(\gamma M_s H_{ac}^2/\rho), \qquad H_{ac} < \alpha H_{dc}, \quad (14a)$$

$$\bar{Q}_{res} = \alpha(\gamma M_s H_{dc}^2/\rho), \qquad H_{ac} \geq \alpha H_{dc}. \quad (14b)$$

The analytical calculations (the solid lines) of Eq. (14) are in excellent agreement with the simulation results (the

symbols) shown in Fig. 7. As shown in Fig. 7(a), the quantity of $\bar{Q}_{res}$ increases with H_{ac} in the form of H_{ac}^2 in the range of $H_{ac} < \alpha H_{dc}$, but it becomes saturated to its maximum value of $\bar{Q}_{res}^{max} = \alpha(\gamma M_s H_{dc}^2/\rho)$ in the range of $H_{ac} \geq \alpha H_{dc}$. This saturated quantity is independent of H_{ac} but increases with H_{dc}^2, as shown in Fig. 7(b). Interestingly, at a certain critical value of $H_{ac} = \alpha H_{dc}$, Eq. (14a) equals Eq. (14b). For $H_{ac} < \alpha H_{dc}$, $\bar{Q}_{res}$ is inversely proportional to α, but for the case of $H_{ac} \geq \alpha H_{dc}$, it proportionally increases with α and H_{dc}^2, as shown in Fig. 7. According to the given values of H_{ac} and H_{dc}, $\bar{Q}_{res}$ can vary proportionally or inversely proportionally with α. Therefore, the quantity of $\bar{Q}_{res}$ can be readily manipulated by tuning H_{ac}, H_{dc}, and α. Equations (14a) and (14b)'s benefit is their informing us why $\bar{Q}_{res}$ increases with α up to 0.05 and then decreases with $\alpha = 0.07$, as shown in Fig. 6. For the given condition imparted by $H_{ac} = 5$ Oe and $H_{dc} = 100$ Oe, $\bar{Q}_{res}$ increases with α for the cases where $\alpha = 0.01$, 0.03, and 0.05, but decreases again when $\alpha = 0.07$, as shown in Fig. 6.

Also, it is indicated that the maximum value of $\bar{Q}_{res}^{max} = \alpha(\gamma M_s H_{dc}^2/\rho)$ under the $H_{ac} \geq \alpha H_{dc}$ condition is the highest energy-dissipation rate at resonance for a given nanosphere in the single-domain state with intrinsic damping parameter α and static field strength H_{dc}. This fact informs us that Gilbert damping is not the only control parameter, but rather that the H_{ac}/H_{dc} ratio is another important factor in obtaining the largest value of $\bar{Q}_{res}$. The quantity of $\bar{Q}_{res}^{max}$ for single-domain Py particles can reach

TABLE I. Comparison of characteristics of three models.

Model	LRT[a]	SWM[a,b]	RSE[c]
Mechanism	Thermal-fluctuation-dominated relaxation	Magnetic anisotropy energy barrier	Resonant precession motion
Main factor	τ_R	H_K	α, H_{dc}
Particle size, D	$D <$ superparamagnetic limit	Superparamagnetic limit $< D <$ single-domain limit	$D <$ single-domain limit
Oscillating field frequency (MHz)	0.01–1	0.01–1	100–1000
Oscillating field amplitude (Oe)	100–1000	100–1000	1–10
SLP (eqs.)	$\lim_{[(K_{eff}V)/(k_BT)]\to 0}\langle Q\rangle = [(H^2_{linear}M_S^2)/6k_BT\rho]$ $[(\omega_{linear}^2\tau_R)/(1+\omega_{linear}^2\tau_R^2)]$ or $\lim_{[(K_{eff}V)/(k_BT)]\to\infty}\langle Q\rangle = [(H^2_{linear}M_S^2)/(2k_BT\rho)]$ $[(\omega_{linear}^2\tau_R)/(1+\omega_{linear}^2\tau_R^2)]$	$\langle Q\rangle = 4f_{linear}H_KM_S/\rho$	$\bar{Q}_{res} = (1/\alpha)(\gamma M_s H_{ac}^2/\rho)$ for $H_{ac} < \alpha H_{dc}$ or $\bar{Q}_{res} = \alpha(\gamma M_s H_{dc}^2/\rho)$ for $H_{ac} \geq \alpha H_{dc}$
Order of SLP (W/g)	Approximately 100	About 1000	About 10 000–100 000

[a]Reference [29].
[b]Reference [19].
[c]This work.

10^4–10^5 W/g, which is 2 or 3 orders of magnitude larger than the typical SLP values of 10^2–10^3 W/g for magnetic hyperthermia based on other mechanisms (Table I). One such mechanism is linear response theory (LRT), which describes the dynamic response of an assembly of magnetic nanoparticles using the Néel-Brown relaxation model. The assumption of this model is that magnetic systems respond linearly with an externally applied magnetic field, as in $\mathbf{M} = \tilde{\chi}\mathbf{H}_{linear}$, where $\tilde{\chi}$ is the complex susceptibility given by $\tilde{\chi} = \chi_0[1/(1 + i\omega_{linear}\tau_R)]$, with χ_0 being the static susceptibility, ω_{linear} the angular frequency of linearly oscillating magnetic field, and τ_R the relaxation time to attainment of the equilibrium state. For aligned magnetic nanoparticles of the zero magnetic anisotropy constant (K_{eff}), the SLP is given as $\langle Q\rangle = [(H^2_{linear}M_S^2)/(6k_BT\rho)] \times [(\omega_{linear}^2\tau_R)/(1+\omega_{linear}^2\tau_R^2)]$, and for aligned magnetic nanoparticles with a strong anisotropy, the SLP is given as $\langle Q\rangle = [(H^2_{linear}M_S^2)/(2k_BT\rho)][(\omega_{linear}^2\tau_R)/(1+\omega_{linear}^2\tau_R^2)]$ for a given temperature T [29]. The LRT model is valid for cases where magnetic nanoparticles are under the superparamagnetic limit, assuming that $[(M_SVH_{linear})/(k_BT)] \ll 1$ and $[(H_{linear})/(H_K)] \ll 1$, as verified in a large number of experimental studies for anisotropy field H_K [19,29–32]. However, for cases where nanoparticles are close to or over the superparamagnetic limit, the LRT model does not work anymore. In cases where the magnetic anisotropy energy barrier of a given material is greater than the thermal fluctuation, i.e., $[(M_SVH_{linear})/(k_BT)] > 1$, the Stoner-Wohlfarth model (SWM) [33] is more valid for a description of the field-dependent magnetic hysteresis loops and the related SLP. Therefore, SLP can be described as $\langle Q\rangle = 4f_{linear}H_KM_S/\rho$. The typical values of SLP are within the range of several hundreds of W/g for the LRT model and

several thousands of W/g for the SWM model [29], as shown in Table I.

The advantage of the resonant spin excitation (RSE) model proposed in this paper is its utilization of resonant magnetization excitations by externally controllable magnetic fields; the other models, contrastingly, are associated with the intrinsic characteristics of materials (e.g., the relaxation time and the magnetic anisotropy field) as key factors in energy dissipation. In our RSE model, the maximum energy-dissipation rate can be achieved and readily controlled using only H_{ac} and H_{dc}, whose strengths are as small as 10^{-2}—an order of magnitude smaller than those of the other models—in order to obtain extremely high values (up to 10^4–10^5 W/g) at resonance when tuning the oscillating field frequency to the Larmor precession frequency. The high energy-dissipation rate obtained in this work opens up a promising line of further research; certainly, if such behavior is confirmed experimentally, it will mean that the use of a small-amplitude ac magnetic field permits considerable energy-dissipation-rate improvement. Also, the suggested RSE model can be extended for a description of energy dissipation in nanoparticles exhibiting superparamagnetic resonance [34,35].

VII. SUMMARY

Using both micromagnetic simulations and analytical derivations, we study in this paper the magnetization dynamics and related energy-dissipation rate of soft magnetic nanospheres in the single-domain state, as excited by rotating magnetic fields under given static magnetic fields. The energy-dissipation rate is found to have its maximum value at resonance in cases where the frequency of the rotating magnetic fields is equal to that of the Larmor precession of uniform magnetizations for a given Gilbert

damping constant. The resonant energy-dissipation rate in the steady state, $\bar{Q}_{\text{res}}$, is simply given in terms of H_{ac} and H_{dc} for a given damping constant. For the cases where $H_{\text{ac}} \geq \alpha H_{\text{dc}}$, the quantity of $\bar{Q}_{\text{res}}$ reaches its maximum value of $\bar{Q}_{\text{res}}^{\max} = \alpha(\gamma M_s H_{\text{dc}}^2/\rho)$. This explicit form provides the highest SLP value, on the order of 10^4–10^5 W/g, and enables ready controllability by externally applied magnetic fields using single-domain magnetic particles in magnetic hyperthermia applications.

This work provides further insights into the fundamentals of magnetization dynamics in magnetic particles and the associated energy-dissipation effect, and it suggests a highly efficient means of magnetic-hyperthermia-applicable energy dissipation.

ACKNOWLEDGMENTS

[1] L. Néel, Thermoremanent magnetization of fine powders, Rev. Mod. Phys. **25**, 293 (1953).

[2] W. F. Brown, Jr., Thermal fluctuations of a single-domain particle, Phys. Rev. **130**, 1677 (1963).

[3] E. M. Chudnovsky, Macroscopic quantum tunneling of the magnetic moment, J. Appl. Phys. **73**, 6697 (1993).

[4] L. Thomas, F. Lionti, R. Ballou, and D. Gatteschi, Macroscopic quantum tunnelling of magnetization in a single crystal of nanomagnets, Nature (London) **383**, 145 (1996).

[5] J. Nogués, J. Sort, V. Langlais, V. Skumryev, S. Surinach, J. Munoz, and M. Baró, Exchange bias in nanostructures, Phys. Rep. **422**, 65 (2005).

[6] C. A. Ross, Patterned magnetic recording media, Annu. Rev. Mater. Res. **31**, 203 (2001).

[7] A. Moser, K. Takano, D. T. Margulies, M. Albrecht, Y. Sonobe, Y. Ikeda, S. Sun, and E. E. Fullerton, Magnetic recording: Advancing into the future, J. Phys. D **35**, R157 (2002).

[8] S. Wolf, D. Awschalom, R. Buhrman, J. Daughton, S. Von Molnar, M. Roukes, A. Y. Chtchelkanova, and D. Treger, Spintronics: A spin-based electronics vision for the future, Science **294**, 1488 (2001).

[9] I. Žutić, J. Fabian, and S. D. Sarma, Spintronics: Fundamentals and applications, Rev. Mod. Phys. **76**, 323 (2004).

[10] T. Shinjo, *Nanomagnetism and Spintronics* (Elsevier, New York, 2013).

[11] Q. A. Pankhurst, J. Connolly, S. K. Jones, and J. Dobson, Applications of magnetic nanoparticles in biomedicine, J. Phys. D **36**, R167 (2003).

[12] V. Labhasetwar and D. L. Leslie-Pelecky, *Biomedical Applications of Nanotechnology* (John Wiley & Sons, New York, 2007).

[13] M. Ferrari, Cancer nanotechnology: Opportunities and challenges, Nat. Rev. Cancer **5**, 161 (2005).

[14] J. Gao, H. Gu, and B. Xu, Multifunctional magnetic nanoparticles: Design, synthesis, and biomedical applications, Acc. Chem. Res. **42**, 1097 (2009).

[15] S.-K. Kim, M.-W. Yoo, J.-H. Lee, Y. Gaididei, V. P. Kravchuk, and D. D. Sheka, Resonantly exited precession motion of three-dimensional vortex core in magnetic nanospheres, Sci. Rep. **5**, 11370 (2015).

[16] S.-K. Kim, M.-W. Yoo, J. Lee, J.-H. Lee, and M.-K. Kim, Resonant vortex-core reversal in magnetic nano-spheres as robust mechanism of efficient energy absorption and emission, Sci. Rep. **6**, 31513 (2016).

[17] T. Neuberger, B. Schöpf, H. Hofmann, M. Hofmann, and B. Von Rechenberg, Superparamagnetic nanoparticles for biomedical applications: Possibilities and limitations of a new drug delivery system, J. Magn. Magn. Mater. **293**, 483 (2005).

[18] M. Shliomis, Magnetic fluids, Phys. Usp. **17**, 153 (1974).

[19] R. Hergt, S. Dutz, R. Müller, and M. Zeisberger, Magnetic particle hyperthermia: Nanoparticle magnetism and materials development for cancer therapy, J. Phys. Condens. Matter **18**, S2919 (2006).

[20] T. Schrefl and J. Fidler, 3D calculation of magnetization processes in Co/Pt multilayers, J. Magn. Magn. Mater. **155**, 389 (1996).

[21] A. S. Szalay, J. Gray, G. Fekete, P. Z. Kunszt, P. Kukol, and A. Thakar, Indexing the sphere with the hierarchical triangular mesh, Microsoft Report No. MSR-TR-2005-123, 2005.

[22] J. A. Osborn, Demagnetizing factors of the general ellipsoid, Phys. Rev. **67**, 351 (1945).

[23] C. Kittel, Ferromagnetic resonance, J. Phys. Radium **12**, 291 (1951).

[24] P. De Châtel, I. Nándori, J. Hakl, S. Mészáros, and K. Vad, Magnetic particle hyperthermia: Néel relaxation in magnetic nanoparticles under circularly polarized field, J. Phys. Condens. Matter **21**, 124202 (2009).

[25] I. Nándori and J. Rácz, Magnetic particle hyperthermia: Power losses under circularly polarized field in anisotropic nanoparticles, Phys. Rev. E **86**, 061404 (2012).

[26] T. Lyutyy, S. Denisov, A. Y. Peletskyi, and C. Binns, Energy dissipation in single-domain ferromagnetic nanoparticles: Dynamical approach, Phys. Rev. B **91**, 054425 (2015).

[27] S. I. Denisov, T. V. Lyutyy, P. Hänggi, and K. N. Trohidou, Dynamical and thermal effects in nanoparticle systems driven by a rotating magnetic field, Phys. Rev. B **74**, 104406 (2006).

[28] T. Roubíček, G. Tomassetti, and C. Zanini, The Gilbert equation with dry-friction-type damping, J. Math. Anal. Appl. **355**, 453 (2009).

[29] J. Carrey, B. Mehdaoui, and M. Respaud, Simple models for dynamic hysteresis loop calculations of magnetic single-domain nanoparticles: Application to magnetic hyperthermia optimization, J. Appl. Phys. **109**, 083921 (2011).

[30] R. Hiergeist, W. Andrä, N. Buske, R. Hergt, I. Hilger, U. Richter, and W. Kaiser, Application of magnetite ferrofluids for hyperthermia, J. Magn. Magn. Mater. **201**, 420 (1999).

[31] X. Wang, H. Gub, and Z. Yang, The heating effect of magnetic fluids in an alternating magnetic field, J. Magn. Magn. Mater. **293**, 334 (2005).

[32] B. Mehdaoui, A. Meffre, L.-M. Lacroix, J. Carrey, S. Lachaize, M. Respaud, M. Gougeon, and B. Chaudret, Large specific absorption rates in the magnetic hyperthermia properties of metallic iron nanocubes, J. Appl. Phys. **107**, 09A324 (2010).

[33] E. C. Stoner and E. P. Wohlfarth, A mechanism of magnetic hysteresis in heterogeneous alloys, Phil. Trans. R. Soc. A **240**, 599 (1948).

[34] R. Berger, J. Kliava, J. C. Bissey, and V. Baïetto, Superparamagnetic resonance of annealed iron-containing borate glass, J. Phys. Condens. Matter **10**, 8559 (1998).

[35] S. V. Titov, P.-M. Dejardin, H. El Mrabti, and Y. P. Kalmykov, Nonlinear magnetization relaxation of superparamagnetic nanoparticles in superimposed ac and dc magnetic bias fields, Phys. Rev. B **82**, 100413(R) (2010).